Anisotropic strain in epitaxial single-layer molybdenum disulfide on Ag(110)†

Luca Bignardi, ✶a,b Sanjoy K. Mahatha, ‡c Daniel Lizzit, §b Harsh Bana, ¶a
Elisabetta Travaglia, ‖a Paolo Lacovig, b Charlotte Sanders, ✶✶c
Alessandro Baraldi, a,b,d Philip Hofmann ✶c and Silvano Lizzit ✶b

In this work we prove that ordered single-layer MoS_2 can be grown epitaxially on Ag(110), despite the different crystalline geometry of adsorbate and substrate. A comprehensive investigation of electronic and structural features of this interface is carried out by combining several techniques. Photoelectron diffraction experiments show that only two mirror crystalline domains coexist in equal amount in the grown layer. Angle-resolved valence band photoelectron spectroscopy shows that MoS_2 undergoes a semi-conductor-to-metal transition. Low-energy electron diffraction and scanning-tunneling microscopy experiments reveal the formation of a commensurate moiré superlattice at the interface, which implies an anisotropic uniaxial strain of the MoS_2 crystalline lattice of *ca.* 3% in the [1$\bar{1}$0] direction of the Ag(110) surface. These outcomes suggest that the epitaxial growth on anisotropic substrates might be an effective and scalable method to generate a controlled and homogeneous strain in MoS_2 and possibly other transition-metal dichalcogenides.

1. Introduction

Two-dimensional transition-metal dichalcogenides (TMDCs) form a group of materials that have attracted a considerable interest in the last years. The various electronic and optical properties in their single or multilayer form, which can be remarkably different from those of their bulk parent compound, have paved the road for a plethora of novel appli-cations, both using the materials in their pristine form and combining them with other two-dimensional (2D) materials to form heterostructures.[1–5] In this broad family, the semi-con-ducting molybdenum disulfide (MoS_2) and tungsten disulfide (WS_2) have been specifically used to explore new logic and computation paradigms to go beyond charge-based devices by exploitation of the valley degree of freedom.[6–9]

The introduction of controlled structural modifications in the crystalline lattice by means of compression or strain has been regarded as a promising strategy to tailor the electronic properties of 2D materials. In particular, the possibility to introduce a strain by an apt choice of the substrate onto which the 2D material is directly grown is probably the most scalable and versatile method to ensure that the strain takes place uni-formly in every region of the interface. This strategy was indi-viduated as an effective way to open a band-gap in graphene electronic structure,[10] markedly showing that the choice of the substrate and of its crystalline arrangement can significantly alter the electronic and structural properties of the supported 2D material.[11–14] Such approach can be successfully extended also to single-layer (SL) TMDCs, which could lead to the con-trolled manipulation of the electronic and optical properties, a desirable achievements in order to use TMDCs in nano-elec-tronics and optoelectronics.[15–26] In this framework, an attrac-tive way to introduce a strain in the crystalline structure of single-layer (SL) TMDCs is to grow the single layer on a sub-strate with different crystalline symmetry than the overlayer and different lattice parameters along distinct crystallographic

*aDepartment of Physics, University of Trieste, via Valerio 2, 34127 Trieste, Italy.
E-mail: lbignardi@units.it*

*bElettra Sincrotrone Trieste, Strada Statale 14 km. 163.5 in AREA Science Park,
34149 Trieste, Italy. E-mail: lizzit@elettra.eu*

*cDepartment of Physics and Astronomy, Interdisciplinary Nanoscience Center
(iNANO), Aarhus University, Ny Munkegade 120, 8000 Aarhus C, Denmark.
E-mail: philip@phys.au.dk*

*dIOM-CNR, Laboratorio TASC, AREA Science Park, Strada Statale 14, km. 163.5,
34149 Trieste, Italy*

‡Present address: School of Physics and Materials Science, Thapar Institute of
Engineering and Technology, Patiala – 147004, India.

§Present address: Dipartimento Politecnico di Ingegneria e Architettura,
University of Udine, 33100 Udine, Italy.

¶Present address: Quantum Solid State Physics, KU Leuven, 3001 Leuven,
Belgium.

‖Present address: IOM-CNR, Laboratorio TASC, AREA Science Park, Strada
Statale 14, km. 163.5, 34149 Trieste, Italy.

✶✶Present address: STFC Central Laser Facility, Research Complex at Harwell,
Harwell Campus, Didcot OX11 0QX UK.

directions.[27–33] Previous studies have highlighted the effect of an additional periodic potential, due to the moiré superlattice, on the electronic properties of graphene and single-layer hexagonal boron nitride grown on anisotropic substrates.[30,34–37] Such outcomes motivated us to explore the effects on the structural and electronic properties of SL MoS_2 grown on a Ag(110) single crystal, which has a rectangular lattice as opposed to the hexagonal lattice of MoS_2. One of the major challenges in the epitaxial growth of TMDCs on surfaces is to avoid the growth of randomly rotated crystalline domains, which might impair the properties of the SL layer. This is commonly happening on substrates weakly interacting with the TMDC single layer, such as graphene,[38–41] silicon oxide[42] or sapphire.[43] To overcome this issue, the use of strong interfacial interactions has previously been identified as a viable solution to achieve well-oriented domains of other SL systems, such as graphene and h-BN on strongly interacting transition metal substrates.[36,44] Semiconducting TMDC, such as WS_2 and MoS_2, upon suitable choice of metal substrate and growth conditions can be grown with a single crystalline orientation or anyway with a high degree of ordering, with important repercussions for the exploitation of the valleytronics-related properties of these materials.[45–51] In the case described in this paper, the choice of Ag(110) substrate was based on the fact that the relatively strong interfacial interactions[52] may suppress the formation of rotated domains.

In this paper, we report on the epitaxial growth of SL MoS_2 on a Ag(110) substrate. Combining several experimental techniques, namely X-ray photoelectron spectroscopy (XPS), Angle-resolved valence-band photoelectron spectroscopy (ARPES), X-ray photoelectron diffraction (XPD), low-energy electron diffraction (LEED) and scanning-tunneling microscopy (STM), we provide a comprehensive characterization of this interface from a point of view of the interface morphology and the electronic structure.

2. Experimental details

2.1 Sample preparation

The growth experiments were performed at SuperESCA beamline of the Elettra synchrotron-radiation facility.[53] The Ag(110) crystal was initially cleaned by repeated cycles of Ar^+ sputtering at 1 keV, followed by annealing at 800 K for 10 minutes. Sample cleanliness was confirmed by XPS, which did not show any contaminants.

The MoS_2 single layer was grown by evaporating Mo atoms from a current-heated Mo filament placed in front of the Ag substrate in a H_2S atmosphere. In order to avoid the formation of randomly-oriented crystalline domains in the MoS_2 layer, a new strategy of growth has been devised, consisting in an initial seeding of MoS_2 crystallites, for a coverage of *ca.* 0.07 ML. This was obtained by dosing Mo atoms in a H_2S background pressure at room temperature followed by an annealing at 800 K while turning off the Mo doser. The growth was then continued by evaporating Mo in H_2S atmosphere, keeping the

sample always at 800 K, up to a final coverage of *ca.* 0.75 ML. The Mo deposition rate was about 4.7×10^{-3} ML min^{-1}, with a H_2S pressure of 5×10^{-7} mbar. A monolayer (ML) is defined as one complete layer of MoS_2 on Ag(110), amounting to Mo surface density of 1.15×10^{15} atoms per cm^2, with a MoS_2 lattice parameter of 3.15 Å.

2.2 Experimental methods

High-resolution XPS S 2p and Mo 3d core-level spectra were measured *in situ* at room temperature in normal electron emission on the as-grown MoS_2 SL. The overall energy resolution was below 50 meV. The binding energy of core level spectra was normalized to the position of the Fermi level of the Ag sample. The fit of the data was performed using Doniach–Šunjić function convoluted with Gaussian broadening and a linear background.[54]

Each XPD pattern was obtained by collecting more than 1000 core-level spectra in the region of interest, measured in 50 azimuthal scans ranging the polar emission angles θ, from grazing emission ($\theta = 70°$) to normal emission ($\theta = 0°$). An azimuthal scan consists in the acquisition of the Mo 3d$_{5/2}$, S 2p$_{3/2}$ or Ag 3d$_{5/2}$ core level over a wide azimuthal sector ($\phi = 130°$). For each of these spectra, a peak fit analysis was performed and the intensity $I(\theta, \phi)$ of each component resulting from the fit, *i.e.* the area under the photoemission line, was extracted. The resulting XPD pattern is the azimuthal equidistant polar projection of the modulation function χ defined as:

$$\chi = \frac{I(\theta, \phi) - I_0(\theta)}{I_0(\theta)}, \tag{1}$$

where $I_0(\theta)$ is the average intensity for each azimuthal scan at polar angle θ. The structural determination was performed by comparing measured XPD patterns to multiple scattering simulations for a trial structure. Such patterns were simulated using the program package for Electron Diffraction in Atomic Clusters (EDAC).[55] The presence of two mirror domain orientations was taken into account by an incoherent superposition of the calculated intensities. The agreement between the simulations and the experimental results can be quantified by computing the reliability factor (R):[56]

$$R = \frac{\sum_i (\chi_{\exp,i} - \chi_{sim,i})^2}{\sum_i (\chi_{\exp,i}^2 + \chi_{sim,i}^2)}, \tag{2}$$

where $\chi_{sim,i}$ and $\chi_{\exp,i}$ are the simulated and the experimental modulation functions for each emission angle i. The estimation of the accuracy of the percentage of mirror domains derived by means of R-factor analysis was deduced from the R-factor confidence interval defined as:[57]

$$\Delta R_{\min} = R_{\min} \sqrt{\frac{2}{N}}, \tag{3}$$

where $R_{\min}$ is the minimum R-factor value and N is the number of well-resolved peaks in the XPD pattern ($N \sim 350$), *i.e.* the approximate number of peaks considering the whole

50 azimuthal scans acquired at different polar emission angles.

STM measurements were carried out at the CoSMoS facility at Elettra Sincrotrone Trieste. The images were acquired at room temperature with a SPECS STM 150 Aarhus instrument equipped with a W tip. The samples were transferred through air from the growth chamber to the STM chamber, where they were subsequently annealed up to *ca.* 800 K for 30 min. The Gwyddion free software was used for STM data visualization and analysis.[58]

LEED measurements were carried out using a commercial VG instrument installed at the experimental chamber of the SuperESCA beamline.

ARPES measurements were performed at the SGM-3 beamline[59] of the synchrotron radiation facility ASTRID2 in Aarhus with the sample kept at about 30 K. The energy and angular resolution are better than 30 meV and 0.2°, respectively. The samples were transferred through air from the growth chamber to ARPES chamber, where they were subsequently annealed up to *ca.* 800 K for 30 min.

3. Results and discussion

SL MoS_2 was prepared in UHV by following a two-step procedure, in which a MoS_2 nucleation phase is followed by the direct growth up to the coverage of about 0.75 monolayer (ML). The calibration of the coverage is described in the ESI.† Growth strategies relying on a two-step approach have been already described and proven successful for the layer-by-layer growth of thin films.[60,61] In our experiment, the first step consists in Mo deposition with a background pressure of H_2S ($p = 5 \times 10^{-7}$ mbar) at room temperature, followed by a thermal annealing up to 800 K, still in H_2S background pressure. The final coverage reached after this initial step was about 0.07 ML. Subsequently, we dosed Mo while keeping the substrate at 800 K with the same H_2S pressure used in the first step. The preparation of the SL MoS_2 can be monitored by means of fast XPS, ensuring that only the desired species appear on the surface. It is interesting to report that any attempt to grow SL MoS_2 on Ag(110) with a one-step procedure similar to what successfully accomplished for (111) surfaces of noble metals[45,62] resulted in a single layer with several rotated domains (see ESI† for more details).

High-resolution XPS provides information about the nature of the grown SL (Fig. 1). The Mo 3d (Fig. 1a) and S 2p (Fig. 1b) core levels were acquired with a photon energy $h\nu$ of 360 and 260 eV, respectively. The analysis of Mo 3d spectrum shows the Mo $3d_{5/2}$ centered at a binding energy (BE) of 229.33 eV, with its spin-orbit doublet component (Mo $3d_{3/2}$) shifted by 3.15 eV towards higher BE. The BE of the main peak is found to be slightly higher than that observed for SL MoS_2 on Au(111),[45] with a higher asymmetry parameter $\alpha = 0.08$, too. In Table S1 in ESI† we provide full details about the line shape of Mo 3d and S 2p. This result suggests a semiconductor-to-metal transition of the MoS_2 layer on Ag(110), similar to the case of WS_2/Ag(111).[63]
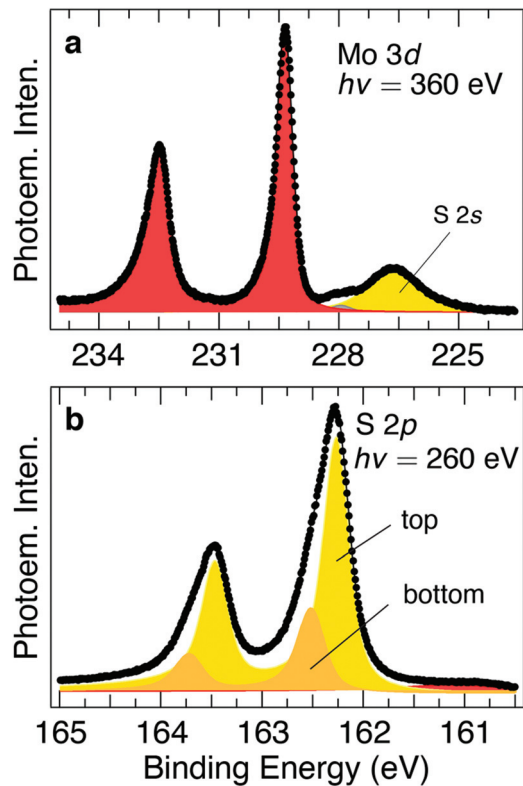

Fig. 1 High-resolution XPS of the (a) Mo 3d and (b) S 2p core levels, respectively, measured after the growth of MoS_2 on Ag(110). The experimental data (dots) and the fit (line) are presented together with the spectral contributions (solid fill) resulting from peak–fitting analysis.

The S 2p core level shows two spin-orbit doublets, with the $2p_{3/2}$ components at 162.27 eV and 162.51 eV BE, respectively. These two components are assigned to S atoms in the top and bottom layer (*i.e.* in contact with the Ag substrate) of the MoS_2 structure, a feature already observed for MoS_2[45] and WS_2[62] on Au(111).

Information about the structural configuration of the interface at the atomic level were obtained by STM experiments. In Fig. 2a, a large scale STM image shows the morphology of the Ag(110) surface, observable in the form of terraces and steps. In contrast to the observation of moiré-induced bright protrusions for MoS_2 on Au(111), no such indication of MoS_2 is directly visible at this scale. However, an atomically-resolved STM image (Fig. 2b), acquired in the region indicated by the white box in panel (a), shows the hexagonally arranged topmost layer S atoms of MoS_2, together with the appearance of a moiré superstructure. The moiré-induced features markedly appear to be misaligned with respect to the rows of S atoms. This is more evident by taking the 2D Fourier transform (2DFT) of this image, from which it is possible to determine the angle of rotation of the moiré superstructure with respect to the MoS_2 lattice. As shown in Fig. 2c, a rectangular arrangement of satellite spots can be observed around each of the spots associated with the lattice parameter of MoS_2. These spots are rotated with respect to the MoS_2 lattice by an angle of 30°.
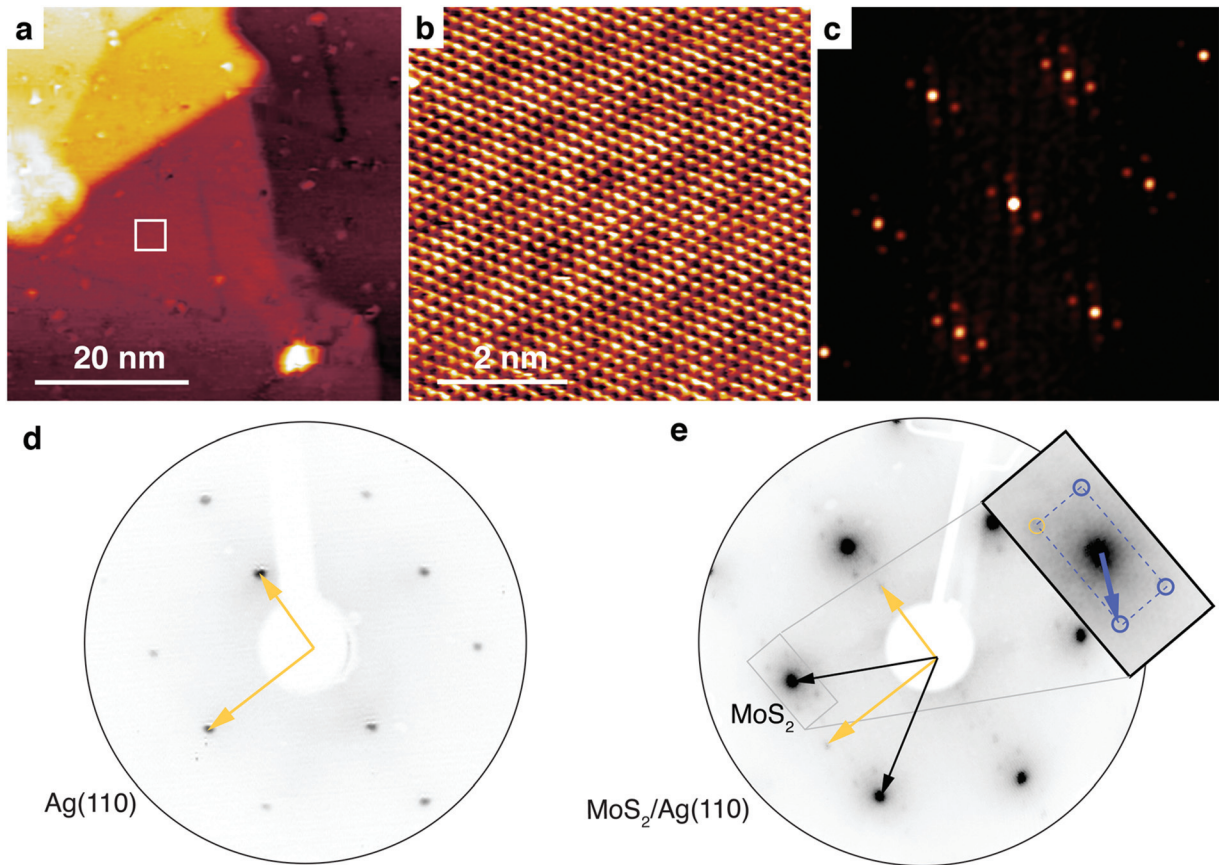
Fig. 2 (a) Large scale STM topography of MoS_2 on Ag(110) (V_B = −1250 mV, I_T = 0.06 nA). (b) Atomically resolved STM image acquired in the region highlighted by the white frame in (a), showing a moiré superstructure (V_B = −740 mV, I_T = 1.51 nA). (c) 2D Fourier Transform of the STM image shown in (b). LEED patterns (d) of the clean Ag(110) sample and (e) of SL MoS_2/Ag(110), both acquired at 120 eV. The diffraction spots corresponding to MoS_2 (black) and Ag(110) (yellow) are indicated. The inset in panel (e) shows a magnification around the (10) spot of MoS_2 highlighting the moiré-induced diffraction spots (blue). The arrow is the reciprocal lattice vector associated with the moiré superstructure.

The acquisition of LEED patterns, shown in Fig. 2d, provides more details about the long-range ordering of the SL MoS_2, and confirms the outcomes observed by means of STM. The principal spots from the MoS_2 ad-layer are visible, together with the principal spots originating from the Ag(110) substrate. The latter can be clearly identified by a direct comparison with a LEED pattern (Fig. 2c) acquired on the clean Ag(110) sample at the same electron energy. Given the three-fold symmetry of the SL MoS_2 crystalline structure, the observation of nearly six-fold symmetry in the intensity of the MoS_2 spots at all beam energies suggests the presence of an equal proportion of mirror domain orientations of MoS_2, although a more thorough analysis about domain orientations requires a different spectroscopic technique such as XPD. In addition to this, the MoS_2 spots are accompanied by satellite spots arranged in a rectangular pattern (marked with the dashed light blue rectangle, see inset in Fig. 2d), which indicates the formation of the moiré superstructure, in agreement with the 2DFT derived from STM topography. The moiré spots have a direction that is rotated of 30° with respect to the main crystallographic directions of the MoS_2 lattice. Moreover, we observe that the moiré is commensurate, with a periodicity corresponding to five times and two times of the lattice parameters of the Ag(110) surface along the [$1\bar{1}0$] and [001] directions of the substrate, respectively.

By combining the results stemming from STM and LEED we can draw a model for the MoS_2/Ag(110) interface, which is reported in Fig. 3. In this configuration, we assume that at the corner of the moiré supercell the S atoms are sitting in a-top sites of the Ag substrate. Such assumption was found to be valid for the case of growth of MoS_2 and WS_2 on Au(111).[45,62] This model can be directly compared with the atomically resolved STM image next to it, where the periodicity and orientation of the moiré superstructure (blue arrows) is also indicated. In order to achieve this periodicity and thus to have the commensurate adsorption configuration that was deduced from STM and LEED analysis, the MoS_2 lattice vector aligned along the [$1\bar{1}0$] direction of the Ag(110) substrate has to be stretched up to 3.23 Å, indicating an expansion of *ca.* 3% in that direction, while the other lattice vector remains unaltered (3.15 Å) with respect to the value reported in literature.[45,64]

As mentioned earlier, an important feature that characterizes epitaxially-grown SL TMDCs is the presence of mirror-oriented crystalline domains. A very versatile tool to obtain
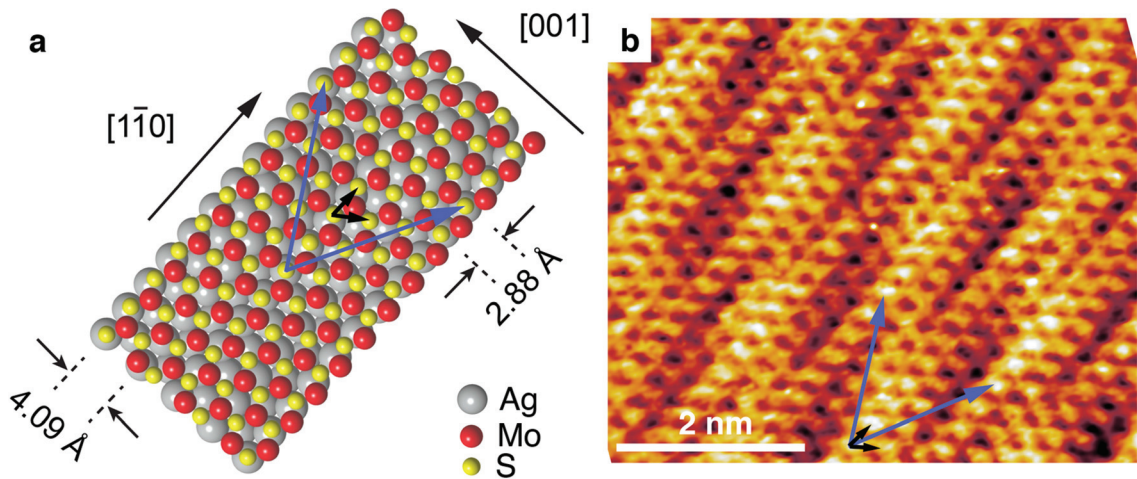
Fig. 3 (a) Structural model of the MoS$_2$/Ag(110) interface. The lattice parameters of Ag(110) along the two main crystallographic directions are also indicated. The MoS$_2$ and moiré lattice vectors are indicated with black and blue arrows, respectively. (b) STM atomic resolution image (V_B = 1200 mV, I_T = 2.05 nA) showing the MoS$_2$ layer (black) and the moiré lattice vectors (light blue).

information at this level is XPD, which has been proven already extremely powerful in determining the local crystalline structure of TMDCs and can be immediately individuate mirror-oriented domains in the crystalline layer.[45,62,65,66] In this experiment, we acquired Mo 3d and S 2p core levels and evaluated their intensity for different emission angles (θ, ϕ).

The experimental XPD patterns obtained are shown in Fig. 4 (in color) and are reported together with simulated patterns obtained via multiple scattering calculations[55] from a test structure (grey). XPD analysis proceeds by finding the best agreement between the experimental and simulated XPD patterns via a R-factor analysis,[56] thus tracing the crystalline struc-
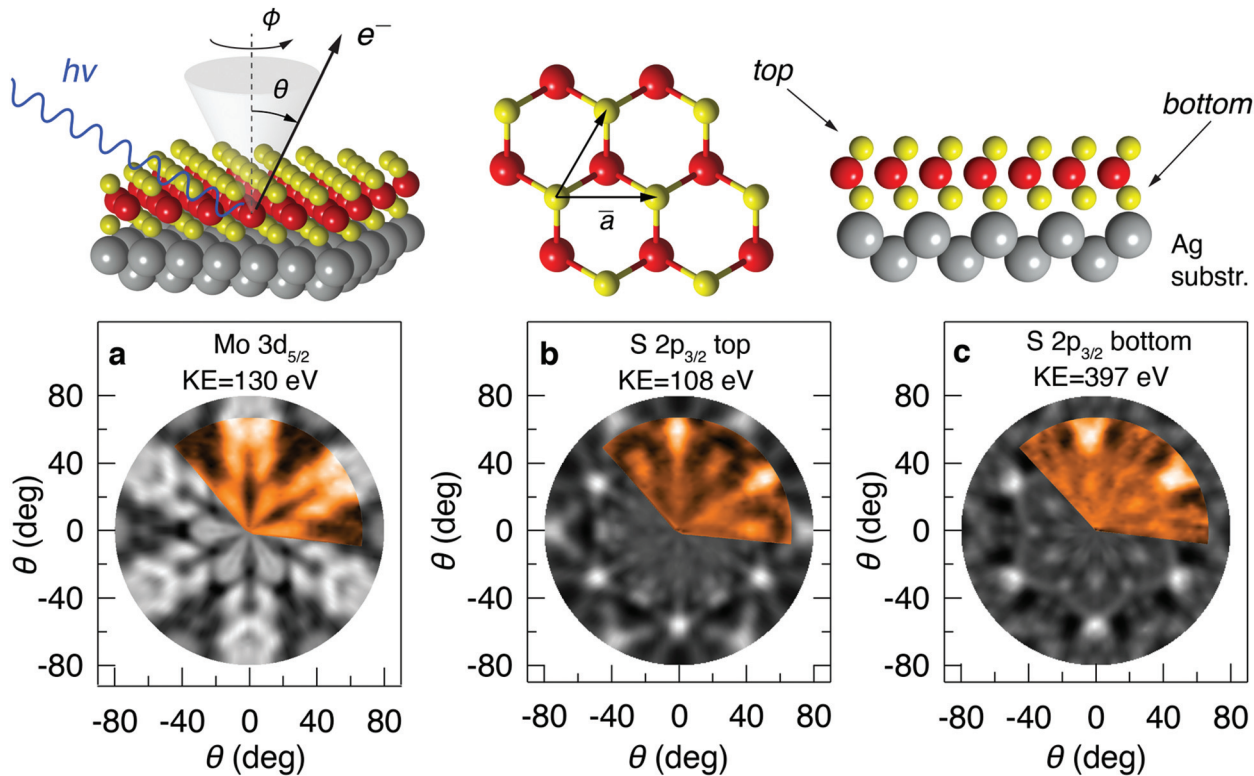

Fig. 4 (a) Experimental Mo 3d$_{5/2}$ XPD pattern (color) obtained at 360 eV photon energy (photoelectron kinetic energy, KE = 130 eV) for the MoS$_2$ single layer together with simulated pattern (grey). XPD pattern for (b) top and (c) bottom S 2p$_{3/2}$ components, acquired at 270 eV photon energy (KE = 108 eV) and 560 eV photon energy (KE = 397 eV), respectively. The experimental data (color) are presented together with the simulated patterns (grey).

ture returning the best correspondence between experiments and simulation. At this stage, the presence of the substrate is neglected due to the lack of specific local adsorption configuration of MoS_2 layer on Ag(110), and hence the simulations were performed for a freestanding MoS_2 layer having the 1H phase structure.[45] These simulations were performed with lattice parameter of 3.15 Å and Mo–S interlayer distance of 1.62 Å.[45] A supporting evidence that the MoS_2 layer is aligned with one of the two crystallographic directions of the Ag(110) substrate, as already observed in LEED, can be obtained by performing XPD measurements to determine the orientation of the substrate, namely acquiring the Ag $3d_{5/2}$ core level (see ESI†).

In order to quantify the relative contribution of different domain orientations in the grown layer, we acquired XPD patterns sourcing from Mo $3d_{5/2}$ core level, Fig. 4a, and compared them with simulated patterns of the Mo 3d core level (photoelectron kinetic energy, KE ~ 130 eV) for two mirror orientations Or1 and Or2, intermixing them in different proportions. In particular, the total measured intensity I_{tot} was expected to be a combination of the I_0 intensity contribution from the main orientation (Or1) and I_{mir} contribution from the mirror orientation (Or2),[45,62,65] such as:

$$I_{tot} = aI_0 + bI_{mir} \quad (b = 1 - a). \tag{4}$$

Fig. 5, central panel, shows the R-factor analysis for the Mo $3d_{5/2}$ XPD pattern: this shows a clear minimum of the R-factor with a percentage of mirror domain orientation of 50(3)%, showing there is an equal coverage of main and mirror orientation in the MoS_2 SL. In addition to that, XPD measurements are performed for the S 2p core level using different photon energies, in order to satisfy the forward (at high KE) and backward scattering (at low KE) conditions. The XPD measurements belonging to top (Fig. 4b) and bottom (Fig. 4c) S 2p components show good agreement with the simulations corresponding to the 1:1 mixture of the two orientations, both for the top layer S (R-factor = 0.24) and bottom layer S

(R-factor = 0.27), respectively. This provides also the confirmation that the polytype of the MoS_2 layer to be 1H.

In order to get further insight into the electronic structure of the interface, we investigated the valence band by means of angle-resolved photoemission spectroscopy (ARPES) measurements, using 30 eV photon energy. In Fig. 6a we plot the photoemission intensity showing the band dispersion along different high symmetry directions of the MoS_2 Brillouin zone (BZ). The characteristic features of single layer MoS_2 are observed, especially the spin-split valence band at $\bar{K}$ and the slightly lower valence band maximum at $\bar{\Gamma}$.[39] The lack of two distinct bands near $\bar{\Gamma}$ confirms the single-layer nature of the grown MoS_2.[67]

As we have seen, the symmetry of the Ag(110) surface does not allow the growth of just one single orientation but it rather favors the growth of mirror-domains that are completely equivalent. However, the interaction between substrate and MoS_2 still has the potential to break the valley degeneracy within the BZ in the material. As seen in Fig. 6c, the $\bar{K}$ and $\bar{K}'$ points of the BZ are no longer equivalent. The spin-split band typical of MoS_2 is observed at the $\bar{K}$ point, with a spin-orbit splitting of 144 meV, similar to that measured for MoS_2 on Au(111).[39,45] Remarkably, the SL MoS_2 valence band maxima at $\bar{K}$ and $\bar{K}'$ (Fig. 6d) appear to be at the same binding energy. This indicates that the effect of the uniaxial strain, of the corrugation of the substrate and of the moiré-induced corrugation is not sufficient to lift the degeneracy in the $\bar{K}$ and $\bar{K}'$ points. Very little changes (few meV) in binding energy might also arise due to inequivalent $\bar{K}$ and $\bar{K}'$ valleys, which we cannot detect.

On the other hand, the upper band at $\bar{K}$ is found at 1.61 eV BE, to be compared with 1.39 eV for MoS_2 on Au(111). The shifted position of the valence band maximum at $\bar{K}$ with respect to the case of Au(111) might be accounted for with the different work function of the Ag(110) substrate with respect to the Au(111). This is reflected also in a shift of the Mo 3d and S 2p core levels towards higher BE, although to a lesser extent.

Interestingly, the faint feature along the $\bar{\Gamma} - \bar{K}$ direction of MoS_2 indicates the presence of additional states close to the Fermi level at the $\bar{Q}$ point, which is further highlighted in the magnified image of the marked region in Fig. 6. This can be
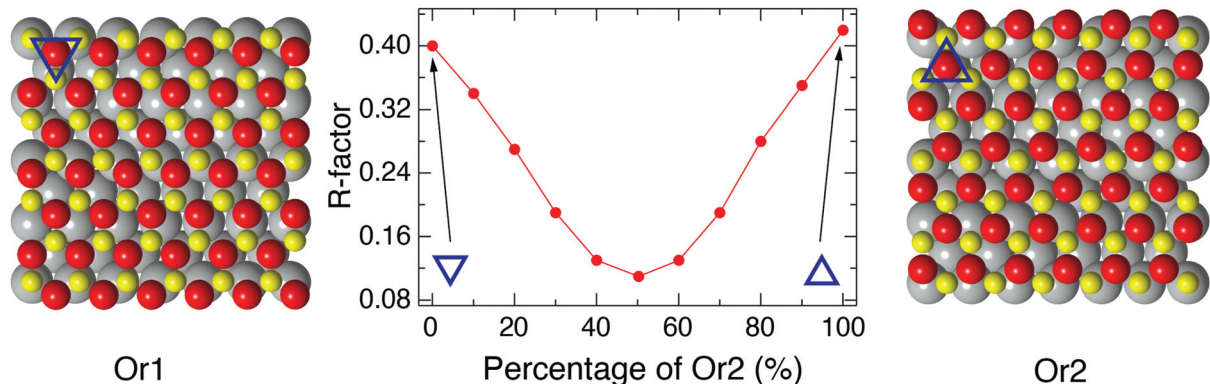

Fig. 5 R-Factor analysis (central panel) for the domain orientation characterization for the Mo $3d_{5/2}$ pattern, revealing the presence of an identical coverage of mirror orientations. The structure for two possible orientations Or1 and Or2 is also shown.
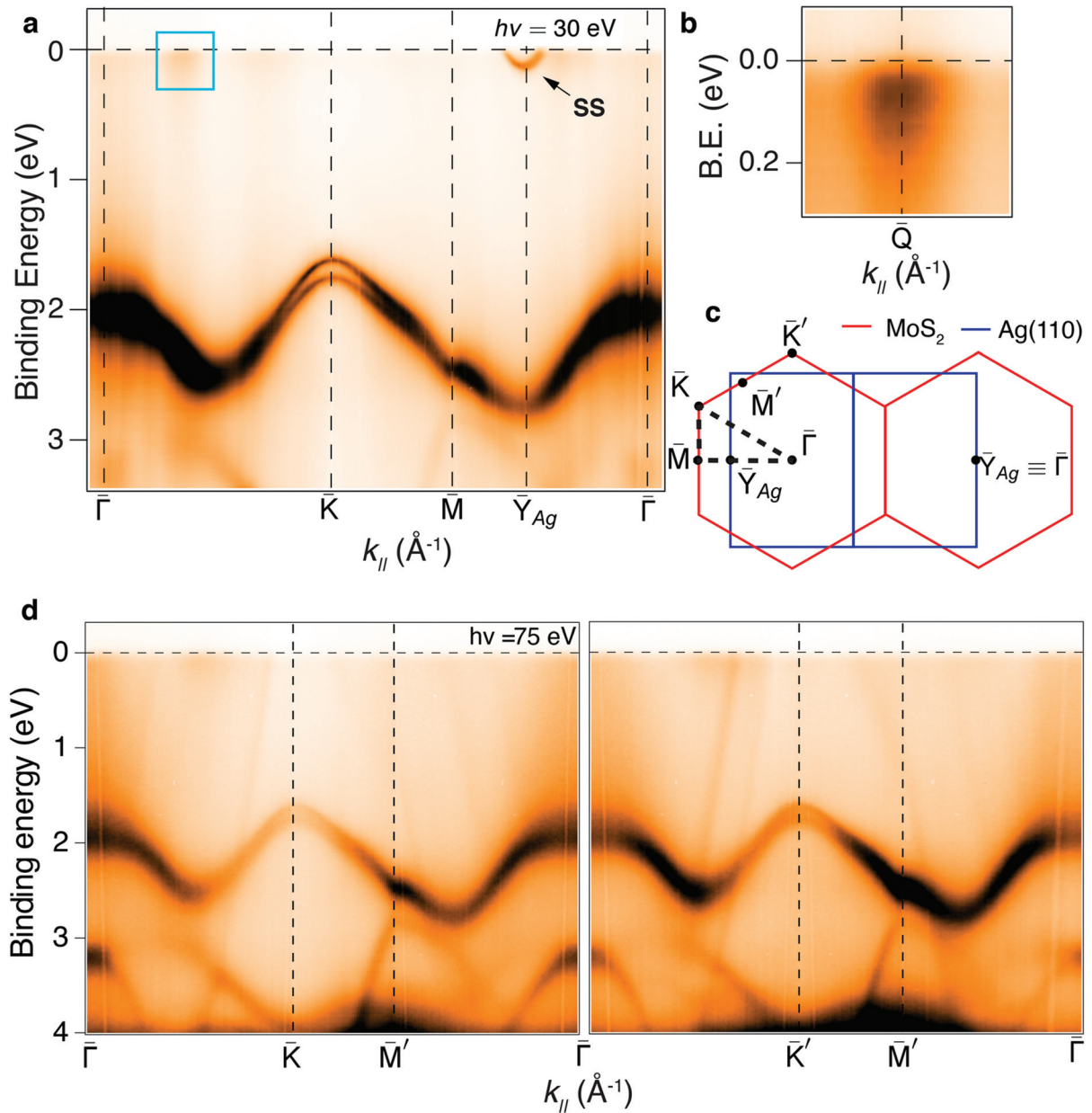
Fig. 6 (a) ARPES spectra acquired on $MoS_2/Ag(110)$ using 30 eV photon energy showing the uppermost MoS_2 valence band and the Ag states, acquired along the path marked in the Brillouin zone scheme on the right. (b) Magnification of the region marked with blue rectangle in (a), showing the additional density of states at the Q point close to the Fermi level. Ag(110) surface state at the Y point of the Brillouin zone is indicated by an arrow in (a). (c) Scheme of the Brillouin zone. (d) ARPES spectra acquired along the $\bar{\Gamma} - \bar{K} - \bar{M}' - \bar{\Gamma}$ and $\bar{\Gamma} - \bar{K}' - \bar{M}' - \bar{\Gamma}$ directions, with a photon energy of 75 eV.

due to the hybridization of the MoS_2 electronic states with those of the underlying Ag substrate, leading to the semiconductor to metal transition of the MoS_2 layer, in agreement with the similar results obtained for WS_2 on Ag(111).[63] This interaction-induced semiconductor-to-metal transition is consistent with the observations we made about the asymmetry of the Mo 3d core level in XPS. In addition to that, we observe a parabolic band at the $\bar{Y}$ point of the Ag(110) surface Brillouin zone. This corresponds to the surface state of Ag(110).

4. Conclusion

We have shown that an ordered MoS_2 single layer can be grown on the anisotropic Ag(110) surface despite the radically different symmetry between substrate and adsorbate. In order to avoid the formation of randomly oriented domains, we have developed a growth strategy that consists of an initial seeding of MoS_2 nano-crystallites, followed by a co-deposition of Mo and S while keeping the substrate at high temperature. The analysis of the high-resolution XPS spectra reveals a high

asymmetry in the line shape of the Mo 3d peak of the MoS_2 layer. The MoS_2 layer presents a high structural quality, as demonstrated by the STM and LEED measurements, where the presence of a moiré superstructure can be also detected. We find that this superstructure, which appears as alternating streaks in the STM topographic images, is misaligned by 30° with respect to the MoS_2 lattice. The MoS_2 appeared to be commensurate with the Ag(110) substrate, which consequently require a stretching of the MoS_2 lattice vector by *ca.* 3% along the closed-packed rows of Ag(110). Based on these findings we propose a model for the MoS_2/Ag(110) interface. XPD measurements show that there is coexistence of MoS_2 crystalline mirror domains in equal proportion, and it is verified that the MoS_2 lattice is, indeed, aligned with the high symmetry [1$\bar{1}$0] direction of the Ag(110) surface. ARPES measurements confirmed that MoS_2 on Ag(110) undergoes a semiconductor-to-metal transition by revealing additional intensity near the Fermi level, at the Q point of Brillouin zone of MoS_2. The indication of the interaction of the MoS_2 single layer with the Ag(110) substrate explain the increased asymmetry in the core-level line shape of Mo 3d. In parallel with that, no differences in the position of the valence band maxima at the $\bar{K}$ and $\bar{K}'$ points are observed, thus suggesting that the moiré-induced corrugation is not capable to lift the degeneracy between K and K′. On the other hand, the characterization of this interface have revealed a simple and direct way to engineer the structure of a SL MoS_2 and induce an uniaxial strain in the crystalline lattice by properly choosing the substrate on which MoS_2 is grown. We envision that this substrate-induced anisotropic strain opens up new possibilities to create strained TMDCs structures, whose peculiar strain-induced physical and chemical properties could find relevant applications in optoelectronics or in driving the catalytic activity of SL TMDCs.[18,20,23,37,68–71] We believe that such approach, similarly to what has been put into practise for graphene, could be extended also to other TMDCs and 2D materials, thus opening up relevant new possibilities in the exploitation of this class of versatile materials.

Conflicts of interest

There are no conflicts to declare.

Acknowledgements

References

1 A. K. Geim and I. V. Grigorieva, *Nature*, 2013, **499**, 419–425.

2 K. S. Novoselov, A. Mishchenko, A. Carvalho and A. H. C. Neto, *Science*, 2016, **353**, aac9439.

3 S.-J. Liang, B. Cheng, X. Cui and F. Miao, *Adv. Mater.*, 2020, **32**, 1903800.

4 K. F. Mak and J. Shan, *Nat. Nanotechnol.*, 2018, **13**, 974–976.

5 M. Chhowalla, H. S. Shin, G. Eda, L.-J. Li, K. P. Loh and H. Zhang, *Nat. Chem.*, 2013, **5**, 263–275.

6 K. F. Mak, C. Lee, J. Hone, J. Shan and T. F. Heinz, *Phys. Rev. Lett.*, 2010, **105**, 136805.

7 K. F. Mak, K. L. McGill, J. Park and P. L. McEuen, *Science*, 2014, **344**, 1489–1492.

8 K. He, C. Poole, K. F. Mak and J. Shan, *Nano Lett.*, 2013, **13**, 2931–2936.

9 H. Zeng, J. Dai, W. Yao, D. Xiao and X. Cui, *Nat. Nanotechnol.*, 2012, **7**, 490–493.

10 F. Guinea, M. I. Katsnelson and A. K. Geim, *Nat. Phys.*, 2010, **6**, 30–33.

11 B. Casarin, A. Cian, Z. Feng, E. Monachino, F. Randi, G. Zamborlini, M. Zonno, E. Miniussi, P. Lacovig, S. Lizzit and A. Baraldi, *J. Phys. Chem. C*, 2014, **118**, 6242–6250.

12 A. Locatelli, C. Wang, C. Africh, N. Stojić, T. O. Menteş, G. Comelli and N. Binggeli, *ACS Nano*, 2013, **7**, 6955–6963.

13 J. M. Wofford, S. Nie, K. F. McCarty, N. C. Bartelt and O. D. Dubon, *Nano Lett.*, 2010, **10**, 4890–4896.

14 E. Monazami, L. Bignardi, P. Rudolf and P. Reinke, *Nano Lett.*, 2015, **15**, 7421–7430.

15 D. Lloyd, X. Liu, J. W. Christopher, L. Cantley, A. Wadehra, B. L. Kim, B. B. Goldberg, A. K. Swan and J. S. Bunch, *Nano Lett.*, 2016, **16**, 5836–5841.

16 M. Li, J. Dai and X. C. Zeng, *Nanoscale*, 2015, **7**, 15385–15391.

17 S. Xie, L. Tu, Y. Han, L. Huang, K. Kang, K. U. Lao, P. Poddar, C. Park, D. A. Muller, R. A. DiStasio and J. Park, *Science*, 2018, **359**, 1131–1136.

18 H. Guo, N. Lu, L. Wang, X. Wu and X. C. Zeng, *J. Phys. Chem. C*, 2014, **118**, 7242–7249.

19 X. Zhao, Z. Ding, J. Chen, J. Dan, S. M. Poh, W. Fu, S. J. Pennycook, W. Zhou and K. P. Loh, *ACS Nano*, 2018, **12**, 1940–1948.

20 R. Roldán, A. Castellanos-Gomez, E. Cappelluti and F. Guinea, *J. Phys.: Condens. Matter*, 2015, **27**, 313201.

21 H. Yu, G.-B. Liu, P. Gong, X. Xu and W. Yao, *Nat. Commun.*, 2014, **5**, 3876.

22 M. Ghorbani-Asl, N. Zibouche, M. Wahiduzzaman, A. F. Oliveira, A. Kuc and T. Heine, *Sci. Rep.*, 2013, **3**, 2691.

23 W. Wei, Y. Dai and B. Huang, *Phys. Chem. Chem. Phys.*, 2016, **19**, 663–672.

24 H. J. Conley, B. Wang, J. I. Ziegler, R. F. Haglund, S. T. Pantelides and K. I. Bolotin, *Nano Lett.*, 2013, **13**, 3626–3630.

25 I. Niehues, A. Blob, T. Stiehm, S. M. de Vasconcellos and R. Bratschitsch, *Nanoscale*, 2019, **11**, 12788–12792.

26 S.-W. Zheng, H.-Y. Wang, L. Wang, Y. Luo, B.-R. Gao and H.-B. Sun, *Nanoscale*, 2021, **13**, 14081–14088.

27 C. Martella, C. Mennucci, A. Lamperti, E. Cappelluti, F. Buatier de Mongeot and A. Molle, *Adv. Mater.*, 2018, **30**, 1705615.

28 C. Martella, C. Mennucci, E. Cinquanta, A. Lamperti, E. Cappelluti, F. Buatier de Mongeot and A. Molle, *Adv. Mater.*, 2017, **29**, 1605785.

29 C. Martella, L. Ortolani, E. Cianci, A. Lamperti, V. Morandi and A. Molle, *Nano Res.*, 2019, **12**, 1851–1854.

30 S. Zhu and H. T. Johnson, *Nanoscale*, 2018, **10**, 20689–20701.

31 Y. Sun, Y. A. Moe, Y. Xu, Y. Sun, X. Wang, F. Li, K. Liu and R. Wang, *Nanoscale*, 2019, **11**, 22432–22439.

32 Y. K. Ryu, R. Frisenda and A. Castellanos-Gomez, *Chem. Commun.*, 2019, **55**, 11498–11510.

33 S. H. Choi, H.-J. Kim, B. Song, Y. I. Kim, G. Han, H. T. T. Nguyen, H. Ko, S. Boandoh, J. H. Choi, C. S. Oh, H. J. Cho, J. W. Jin, Y. S. Won, B. H. Lee, S. J. Yun, B. G. Shin, H. Y. Jeong, Y.-M. Kim, Y.-K. Han, Y. H. Lee, S. M. Kim and K. K. Kim, *Adv. Mater.*, 2021, **33**, 2006601.

34 I. Šrut, V. Mikšić Trontl, P. Pervan and M. Kralj, *Carbon*, 2013, **56**, 193–200.

35 N. A. Vinogradov, A. A. Zakharov, V. Kocevski, J. Rusz, K. A. Simonov, O. Eriksson, A. Mikkelsen, E. Lundgren, A. S. Vinogradov, N. Mårtensson and A. B. Preobrajenski, *Phys. Rev. Lett.*, 2012, **109**, 026101.

36 N. A. Vinogradov, A. A. Zakharov, M. L. Ng, A. Mikkelsen, E. Lundgren, N. Mårtensson and A. B. Preobrajenski, *Langmuir*, 2012, **28**, 1775–1781.

37 C. Hu, V. Michaud-Rioux, W. Yao and H. Guo, *Phys. Rev. Lett.*, 2018, **121**, 186403.

38 Y. Shi, W. Zhou, A.-Y. Lu, W. Fang, Y.-H. Lee, A. L. Hsu, S. M. Kim, K. K. Kim, H. Y. Yang, L.-J. Li, J.-C. Idrobo and J. Kong, *Nano Lett.*, 2012, **12**, 2784–2791.

39 J. A. Miwa, M. Dendzik, S. S. Grønborg, M. Bianchi, J. V. Lauritsen, P. Hofmann and S. Ulstrup, *ACS Nano*, 2015, **9**, 6502–6510.

40 J. Hall, B. Pielić, C. Murray, W. Jolie, T. Wekking, C. Busse, M. Kralj and T. Michely, *2D Mater.*, 2018, **5**, 025005.

41 F. Loi, L. Sbuelz, P. Lacovig, D. Lizzit, L. Bignardi, S. Lizzit and A. Baraldi, *J. Phys. Chem. C*, 2020, **124**, 20889–20897.

42 F. Zhang, K. Momeni, M. A. AlSaud, A. Azizi, M. F. H. Jr, J. M. Redwing, L.-Q. Chen and N. Alem, *2D Mater.*, 2017, **4**, 025029.

43 D. Dumcenco, D. Ovchinnikov, O. L. Sanchez, P. Gillet, D. T. L. Alexander, S. Lazar, A. Radenovic and A. Kis, *2D Mater.*, 2015, **2**, 044005.

44 A. B. Preobrajenski, M. L. Ng, A. S. Vinogradov and N. Mårtensson, *Phys. Rev. B: Condens. Matter Mater. Phys.*, 2008, **78**, 073401.

45 H. Bana, E. Travaglia, L. Bignardi, P. Lacovig, C. E. Sanders, M. Dendzik, M. Michiardi, M. Bianchi, D. Lizzit, F. Presel, D. D. Angelis, N. Apostol, P. K. Das, J. Fujii, I. Vobornik, R. Larciprete, A. Baraldi, P. Hofmann and S. Lizzit, *2D Mater.*, 2018, **5**, 035012.

46 P. Eickholt, C. Sanders, M. Dendzik, L. Bignardi, D. Lizzit, S. Lizzit, A. Bruix, P. Hofmann and M. Donath, *Phys. Rev. Lett.*, 2018, **121**, 136402.

47 H. Beyer, G. Rohde, A. G. Čabo, A. Stange, T. Jacobsen, L. Bignardi, D. Lizzit, P. Lacovig, C. E. Sanders, S. Lizzit, K. Rossnagel, P. Hofmann and M. Bauer, *Phys. Rev. Lett.*, 2019, **123**, 236802.

48 P. Majchrzak, K. Volckaert, A. G. Čabo, D. Biswas, M. Bianchi, S. K. Mahatha, M. Dendzik, F. Andreatta, S. S. Grønborg, I. Marković, J. M. Riley, J. C. Johannsen, D. Lizzit, L. Bignardi, S. Lizzit, C. Cacho, O. Alexander, D. Matselyukh, A. S. Wyatt, R. T. Chapman, E. Springate, J. V. Lauritsen, P. D. King, C. E. Sanders, J. A. Miwa, P. Hofmann and S. Ulstrup, *J. Electron Spectrosc. Relat. Phenom.*, 2021, **250**, 147093.

49 K. Volckaert, H. Rostami, D. Biswas, I. Marković, F. Andreatta, C. E. Sanders, P. Majchrzak, C. Cacho, R. T. Chapman, A. Wyatt, E. Springate, D. Lizzit, L. Bignardi, S. Lizzit, S. K. Mahatha, M. Bianchi, N. Lanata, P. D. C. King, J. A. Miwa, A. V. Balatsky, P. Hofmann and S. Ulstrup, *Phys. Rev. B*, 2019, **100**, 241406.

50 H. Rostami, K. Volckaert, N. Lanata, S. K. Mahatha, C. E. Sanders, M. Bianchi, D. Lizzit, L. Bignardi, S. Lizzit, J. A. Miwa, A. V. Balatsky, P. Hofmann and S. Ulstrup, *Phys. Rev. B*, 2019, **100**, 235423.

51 U. Kamber, S. Pakdel, R.-M. Stan, A. Kamlapure, B. Kiraly, F. Arnold, A. Eich, A. S. Ngankeu, M. Bianchi, J. A. Miwa, C. E. Sanders, N. Lanatà, P. Hofmann and A. A. Khajetoorians, *Phys. Rev. B*, 2021, **103**, 115414.

52 M. Farmanbar and G. Brocks, *Phys. Rev. B*, 2016, **93**, 085304.

53 A. Baraldi, G. Comelli, S. Lizzit, M. Kiskinova and G. Paolucci, *Surf. Sci. Rep.*, 2003, **49**, 169–224.

54 S. Doniach and M. Sunjic, *J. Phys. C: Solid State Phys.*, 1970, **3**, 285–291.

55 F. J. Garcìa de Abajo, M. A. Van Hove and C. S. Fadley, *Phys. Rev. B: Condens. Matter Mater. Phys.*, 2001, **63**, 075404.

56 D. Woodruff, *Surf. Sci. Rep.*, 2007, **62**, 1–38.

57 J. B. Pendry, *J. Phys. C: Solid State Phys.*, 1980, **13**, 937–944.

58 D. Nečas and P. Klapetek, *Cent. Eur. J. Phys.*, 2012, **10**, 181–188.

59 S. V. Hoffmann, C. Søndergaard, C. Schultz, Z. Li and P. Hofmann, *Nucl. Instrum. Methods Phys. Res., Sect. A*, 2004, **523**, 441.

60 B. Loukya, P. Sowjanya, K. Dileep, R. Shipra, S. Kanuri, L. Panchakarla and R. Datta, *J. Cryst. Growth*, 2011, **329**, 20–26.

61 G. Koster, G. J. H. M. Rijnders, D. H. A. Blank and H. Rogalla, *Appl. Phys. Lett.*, 1999, **74**, 3729–3731.

62 L. Bignardi, D. Lizzit, H. Bana, E. Travaglia, P. Lacovig, C. E. Sanders, M. Dendzik, M. Michiardi, M. Bianchi, M. Ewert, L. Buß, J. Falta, J. I. Flege, A. Baraldi, R. Larciprete, P. Hofmann and S. Lizzit, *Phys. Rev. Mater.*, 2019, **3**, 014003.

63 M. Dendzik, A. Bruix, M. Michiardi, A. S. Ngankeu, M. Bianchi, J. A. Miwa, B. Hammer, P. Hofmann and C. E. Sanders, *Phys. Rev. B*, 2017, **96**, 235440.

64 R. Holinski and J. Gänsheimer, *Wear*, 1972, **19**, 329–342.

65 L. Bignardi, P. Lacovig, M. M. Dalmiglio, F. Orlando, A. Ghafari, L. Petaccia, A. Baraldi, R. Larciprete and S. Lizzit, *2D Mater.*, 2017, **4**, 025106.

66 F. Arnold, R.-M. Stan, S. K. Mahatha, H. E. Lund, D. Curcio, M. Dendzik, H. Bana, E. Travaglia, L. Bignardi, P. Lacovig, D. Lizzit, Z. Li, M. Bianchi, J. A. Miwa, M. Bremholm, S. Lizzit, P. Hofmann and C. E. Sanders, *2D Mater.*, 2018, **5**, 045009.

67 S. S. Grønborg, S. Ulstrup, M. Bianchi, M. Dendzik, C. E. Sanders, J. V. Lauritsen, P. Hofmann and J. A. Miwa, *Langmuir*, 2015, **31**, 9700–9706.

68 L. Kou, A. Du, C. Chen and T. Frauenheim, *Nanoscale*, 2014, **6**, 5156–5161.

69 S. A. Khan, B. Amin, L.-Y. Gan and I. Ahmad, *Phys. Chem. Chem. Phys.*, 2017, **19**, 14738–14744.

70 E. Blundo, C. D. Giorgio, G. Pettinari, T. Yildirim, M. Felici, Y. Lu, F. Bobba and A. Polimeni, *Adv. Mater. Interfaces*, 2020, **7**, 2000621.

71 C. Mennucci, A. Mazzanti, C. Martella, A. Lamperti, M. Bhatnagar, R. Lo Savio, L. Repetto, A. Camellini, M. Zavelani-Rossi, A. Molle, F. Buatier de Mongeot and G. Della Valle, *Adv. Opt. Mater.*, 2021, **9**, 2001408.